ADVANCED ENERGY MATERIALS
www.advenergymat.de

Ultrathin, Layer-by-Layer Assembled Lithiophilic Interlayers for Dendritic Growth-Suppressed Lithium Metal Anodes

Donghyeon Nam, Kyuho Jin, Tae Hwan Jo, Chanseok Lee, Keun Hee Kim, Hyewon Kang, Ho Yeon Jang, Younghoon Kim, Seung Woo Lee, Seoin Back, Yongmin Ko,* and Jinhan Cho**

Lithium (Li) metal, recognized for its high energy potential, serves as a promising anode material in battery technologies. However, the growth of Li dendrites during charging and discharging cycles presents significant safety and durability challenges. To address these challenges, a novel strategy is developed employing an ultrathin, layer-by-layer (LbL) assembled multi-walled carbon nanotube forest (MWCF) interlayer that is uniquely composed of lithiophilic components without inactive binders. Strategically deposited on one side of the separator, the LbL-assembled MWCF interlayer ensures excellent electrical conductivity and forms seamless interfaces with the separator, optimizing ion transport and reducing local current density. This configuration allows for uniform Li plating while preventing dendrite penetration toward the cathode, thus enhancing safety and extending the cell's lifespan. This approach has demonstrates exceptional cycling stability, sustaining over 10 000 h of operation at 1 mA cm^{-2} and 1 mAh cm^{-2} in a symmetric Li | Li cell, surpassing previously reported results. Furthermore, an $LiNi_{0.8}Mn_{0.1}Co_{0.1}O_2$-based asymmetric cell exhibits remarkable durability, maintaining ≈81.9% of its capacity after 600 cycles at 1 C, and achieving an ultrahigh energy of 678 Wh Kg^{-1}. An $LiFePO_4$-based asymmetric cell also demonstrates superior cycling stability, further validating the effectiveness of our approach.

1. Introduction

Li metal is considered a highly promising anode material because it has the highest theoretical specific capacity (3860 mAh g^{-1}), an extremely low redox potential (−3.04 V vs SHE), and a very low density (0.534 g cm^{-3}). These properties could help overcome the energy density limits of conventional graphite anodes (372 mAh g^{-1}) in rechargeable Li batteries.[1–4] However, despite these remarkable advantages, serious challenges remain—such as an unstable solid-electrolyte interphase (SEI) layer with insufficient surface coverage, uncontrollable volume fluctuations, and Li dendrite growth. These issues compromise both performance and safety, limiting the practical use of Li metal anodes (LMAs) in batteries.[5,6]

Among the various causes, the non-uniform distribution of current density on the LMA surface and/or

D. Nam, C. Lee, J. Cho
Department of Chemical and Biological Engineering
Korea University
145 Anam-ro, Seongbuk-gu, Seoul 02841, Republic of Korea
E-mail: jinhan71@korea.ac.kr

K. Jin, S. Back, J. Cho
KU-KIST Graduate School of Converging Science & Technology
Korea University
145 Anam-ro, Seongbuk-gu, Seoul 02841, Republic of Korea
E-mail: sback@korea.ac.kr

T. H. Jo, H. Y. Jang
Department of Chemical and Biomolecular Engineering
Sogang University
Baekbeom-ro 35, Mapo-gu, Seoul 04107, Republic of Korea

D. Nam, K. H. Kim, H. Kang, S. W. Lee
The George W. Woodruff School of Mechanical Engineering
Georgia Institute of Technology
Atlanta, GA 30332, USA

Y. Kim
Department of Chemistry
Kookmin University
77 Jeongneung-ro, Seongbuk-gu, Seoul 02707, Republic of Korea

Y. Ko
Division of Energy & Environmental Technology
Materials Research Institute
Daegu Gyeongbuk Institute of Science and Technology (DGIST)
333 Techno Jungang-daero, Hyeonpung-eup, Dalseong-gun, Daegu 42988, Republic of Korea
E-mail: yongmin.ko@dgist.ac.kr

J. Cho
Soft Hybrid Materials Research Center
Advanced Materials Research Division
Korea Institute of Science and Technology (KIST)
Seoul 02792, Republic of Korea

The ORCID identification number(s) for the author(s) of this article can be found under https://doi.org/10.1002/aenm.202500850

DOI: 10.1002/aenm.202500850

LMA/electrolyte interface is widely recognized as a key factor. During charging, Li^+ ions pass through the SEI layer and gain electrons at the anode surface, where they are reduced to form Li metal.[7,8] These Li atoms tend to accumulate at defects or surface irregularities, where the energy is lower, leading to localized growth of Li crystals (nucleation) and eventually forming sharp protrusions—known as Li dendrites.[9,10] This uneven growth stresses the SEI layer, often causing it to crack.[11] The structural fracture of the SEI layer exposes the fresh Li metal, which reacts with the electrolyte and promotes further uncontrolled deposition and SEI growth. This cycle of damage lead to thick, non-uniform SEI layer, needle-like Li dendrites, and continuous volume expansion, all of which degrade the battery's lifespan, efficiency, and safety.[12] Therefore, to prevent dendrite formation and ensure safe, long-lasting batteries, a key strategy is to design electrodes that promote uniform current density and ion distribution across the LMA.

Extensive efforts have been made to reduce the local current density and enhance the stability of the LMA surface through tailored chemical and/or structural design. These efforts encompass the development of organic or inorganic lithiophilic sites, the creation of highly porous frameworks on the host electrodes, and the implementation of hierarchical architectures.[13–19] As another alternative, various types of 3D structures with abundant lithiophilic sites have garnered significant attention for their ability to regulate the current distribution at the LMA/electrolyte interfaces.[20–24] Among them, highly entangled carbon nanotubes (CNTs) could serve as an ideal interlayer material for uniform Li deposition in high-rate LMB applications due to their high electrical conductivity and lower redox potential compared to organic frameworks.[25–27] In particular, the electrical conductivity of such an interlayer structure can act as a pivotal factor in alleviating interfacial resistance on Li^+ ion transport to the surface of the host electrode, enabling low overpotential during the high-rate Li plating process.[28] Additionally, the porous structure of conductive CNT composites can aid in achieving a uniform distribution of the electric field at the electrode/electrolyte interfaces, which effectively regulates the Li^+ ion concentration gradient.[29,30] Furthermore, it should be noted that the spacious 3D network of the CNT architectures adequately buffers volume changes during continuous Li plating and stripping processes.[31] Consequently, numerous strategies based on carbon materials, including CNTs, have been implemented by simply depositing a slurry onto the surface of LMA or the separator.[32,33] However, the inclusion of insulating polymer binders within thick slurry layers (ranging from a few to several tens of μm) can significantly limit the porosity and charge mobility, hindering performance enhancement. Particularly, the thick thickness (or high loading mass) of slurry-based interlayers significantly decreases the energy density of LMBs. As a result, researchers and battery companies are now focusing on developing ultrathin, highly conductive, and lithiophilic interlayers, although an ideal solution has not yet been found.

Moreover, the role of interfacial interactions has often been overlooked. These include interactions between adjacent components (i.e., CNTs and/or lithiophilic species) within the interlayer as well as between the interlayer and substrate (i.e., LMA or separator). Poor interfacial compatibility can lead to aggregation or separation within the layer, resulting in poor connectivity and discontinuous interfaces. These issues create electric field gradients on the interlayer surface, which disrupt ion transport.[34] In short, the design of functional interlayers must carefully consider both physical properties (like thickness, porosity, and density) and interfacial structure, which together affect Li plating behavior and dendrite growth kinetics.[35–38] Therefore, developing an efficient methodological approach to precisely control and optimize these factors is highly desirable.

In this study, we introduce an ultrathin (≈62 nm thick and 16.5 μg cm^{-2} in mass), electrochemically inactive component-free lithiophilic multiwalled-carbon-nanotube-forest (MWCF) designed through a lithiophilic molecular linker-mediated layer-by-layer (LbL) assembly approach on separator (**Scheme 1a**). This innovative yet straightforward methodology enables the creation of a gapless and intimate interface between the lithiophilic MWCF interlayer and the separator. By leveraging nanometer scale-controlled complementary interactions between lithiophilic COOH-functionalized MWCNTs (COOH-MWCNTs) and lithiophilic NH_2-functionalized small molecular linkers (tris(2-aminoethyl) amine, TAA) as well as between NH_2-TAA and separator, this approach effectively regulates the Li dendritic growth on the LMA surface, resulting in unprecedented operational stability. Notably, the lithiophilic molecular linkers directly connect neighboring lithiophilic COOH-MWCNTs with a well-defined interaction, ensuring structural integrity to effectively withstand mechanical (i.e., volume expansion and contraction during electrochemical cycles) and/or electrochemical stresses (i.e., SEI formation, and Li dendrite growth) during repeated Li plating and stripping processes. Our approach also leverages the tailored chemical and physical properties of functional interlayers, assembled at the nanometer scale without insulating polymer binders, to influence the electrochemical kinetics of LMAs through interfacial interactions between two distinct lithiophilic functional components (i.e., COOH groups of MWCNTs and NH_2 groups of molecular linkers).

To achieve this goal, the MWCF was formed through lithiophilic linker-mediated LbL assembly of COOH-MWCNTs and NH_2-TAA onto a commercial battery separator. Importantly, this LbL approach ensures uniform distribution of abundant lithiophilic organic moieties (i.e., oxygen- and nitrogen-containing functional groups) within the conductive MWCF networks, facilitating fast and homogeneous Li^+ ion flux and effectively suppressing irregular Li dendrite growth. In particular, the lithiophilic molecular linker-induced LbL-assembly, excluding bulky/insulating polymeric linkers, enables the formation of a highly entangled ultrathin forest interlayer with a robust interfacial structure without any inactive components, preserving the porous nature and electrical conductivity of the COOH-MWCNT itself. This MWCF interlayer configuration promotes the formation of a uniform Li thin layer at the MWCF/separator interface, directing Li growth toward the LMA surface and preventing its invasion into the separator (Scheme 1b). Using these MWCF interlayer-assembled separators, the resulting symmetric Li | Li cell demonstrated an exceptional lifetime exceeding 10 000 h under a current density of 1 mA cm^{-2} and a capacity of 1 mAh cm^{-2}. Additionally, a full-cell configuration composed of LMA and $LiNi_{0.8}Mn_{0.1}Co_{0.1}O_2$ (NMC811) cathode achieved remarkable cycling stability of 81.9% after 600 cycles at 1 C and

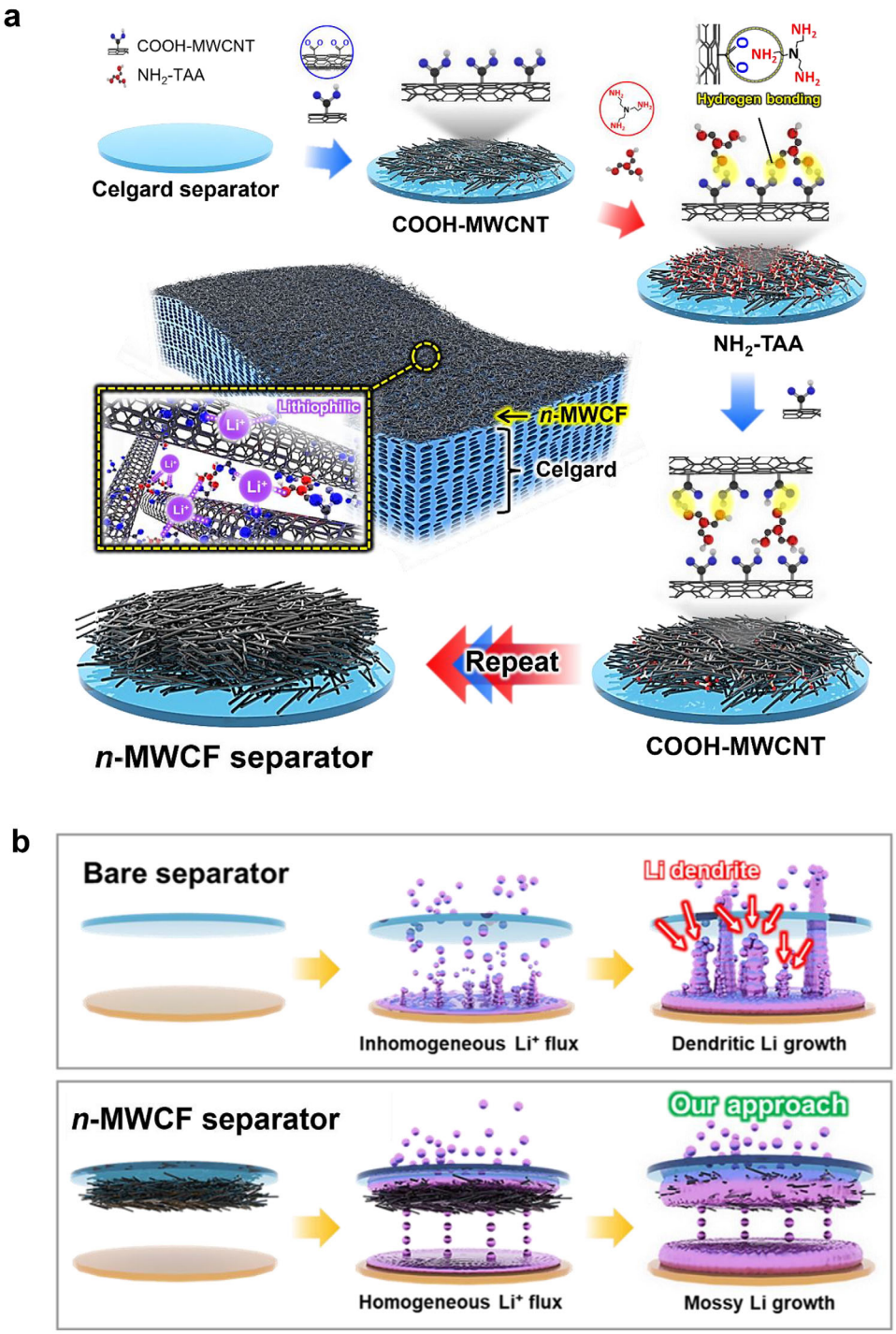

Scheme 1. Schematic illustration a) Schematic illustration for the preparation of *n*−MWCF separator. b) Comparison of Li growth behavior dependent on separators in repetitive galvanostatic Li plating.

delivered a maximal energy density of 678 Wh kg^{-1} at 0.1 mA cm^{-2}. Surprisingly, $LiFePO_4$ (LFP) cathode-employed full cells demonstrated excellent cycling stability of 107% even after 1500 cycles at 1 C. These results significantly outperformed the typical interlayer-based cells reported to date, which are limited by unfavorable interfacial design. As a result, our novel structural and interfacial interaction design offers unprecedented performance in terms of stability and energy density. Therefore, we believe that our approach, which allows precise and straightforward control of the physical and chemical properties of all components and resulting interlayers, offers new insights and a foundation for developing future high-performance LMBs.

2. Results and Discussion

2.1. Preparation of multilayered MWCF

To prepare lithiophilic MWCF, we first transformed pristine hydrophobic MWCNTs to hydrophilic COOH-MWCNTs using H_2SO_4/HNO_3 oxidative method, which induced the formation of COOH moieties on the exterior surface of MWCNTs. The successful surface modification of the resulting COOH-MWCNTs was verified by high dispersion stability in ethanol and by Fourier transform infrared (FTIR) spectroscopy (**Figure** 1a; Figure S1, Supporting Information). In this case, the COOH-MWCNTs maintained their native tubular characteristic without significant fragments after the given oxidation condition (Figure 1b).

Based on these results, the COOH-MWCNTs were sequentially LbL-assembled with NH_2-functionalized TAA (abbreviated as NH_2-TAA, molecular weight ≈146 g mol^{-1}) linkers through hydrogen-bonding interaction between COOH moieties of MWCNTs and NH_2 moieties of TAA in ethanol (Figure 1c). The FTIR spectra of the formed $(NH_2\text{-TAA/COOH-MWCNT})_n$ multilayers exhibited evident absorption peaks originating from the carbonyl (C═O) stretching vibration of COOH moieties at 1704 cm^{-1} and N—H bending vibration of NH_2 moieties at 1573 cm^{-1}, respectively (Figure S1, Supporting Information), and the peak intensities of these characteristic vibrations were gradually intensified as the bilayer number (n) was increased from 1 to 3 (Figure 1d). Further validation of the hydrogen bonding was provided by observing amide bond formation post-thermal treatment and supported by density functional theory (DFT) calculations (Figures S2 and S3, Supporting Information).

The adsorption behavior of $(NH_2\text{-TAA/COOH-MWCNT})_n$ multilayers was also investigated using UV–vis spectroscopy (Figure 1e). With increasing the bilayer number (n) from 1 to 10, the intensity of the absorption spectra was almost linearly increased. In this case, the total film thicknesses of the $(NH_2\text{-TAA/COOH-MWCNT})_n$ multilayers were increased up to ≈198 nm (for $n = 10$), implying that the thickness per bilayer was estimated to be ≈19.8 nm (Figure 1f). The average mass change (Δm) per bilayer was calculated from the frequency change (ΔF) using quartz crystal microbalance (QCM) measurement and estimated to be ≈5.5 μg cm^{-2} ($\Delta F \approx 312$ Hz) (Figure 1g). In this case, the proportion of TAAs within the multilayer is only ≈12.8% (i.e., ≈0.7 μg cm^{-2} per bilayer), affording the advantage of fully harnessing the characteristics of the COOH-MWCNTs, including porous structure and electrical properties. As a result, these observations clearly imply that the adsorbed amount per bilayer was almost regular, and furthermore, could be exactly controlled by the bilayer number (n). Therefore, each component (i.e., COOH-MWCNTs and NH_2-TAAs) can be evenly distributed within the entire region of the resulting LbL-assembled multilayers.

In particular, given that the oxygen atoms within the COOH groups of MWCNTs and the nitrogen atoms within the NH_2 groups of TAA have a strong affinity for Li^+ ions,[39,40] the $(NH_2\text{-TAA/COOH-MWCNT})_n$ multilayers (i.e., n-MWCFs) with a homogeneous structure serve a uniform active sites for Li deposition during electrochemical operations. Since the LbL-assembled multilayers are composed solely of COOH-MWCNTs and NH_2-TAA molecular linkers without electrochemically and lithiophilically inactive components or bulky polymeric linkers, our MWCF is expected to exhibit strong lithiophilic properties, a highly uniform/nanoporous structure, and excellent electrical conductivity. These properties are highly advantageous, facilitating the fast and homogeneous infiltration of Li^+ ions into the MWCFs and effectively suppressing the irregular growth of Li dendrites.

2.2. Characterization of MWCF on Separator

To confirm these possibilities, the MWCFs were deposited onto one side of the UV-irradiated polypropylene (PP) separator (Celgard 2400) using a hydrogen-bonding interaction-mediated LbL assembly. As shown in **Figure** 2a, the surface coverage of the MWCF on the separator gradually increased as the bilayer number (n) of the multilayers increased from 0 to 5. In particular, the 3-MWCFs with a thickness of ≈60 nm exhibited a surface coverage of over 90% on the separator while well-maintaining a highly nanoporous structure (Figure S4, Supporting Information). Furthermore, the formed MWCFs exhibited exceptionally smooth surface morphologies with nanometer-scale roughness, indicating uniform deposition of the components through the LbL assembly process (Figure S5, Supporting Information). These features enable the LbL-assembled MWCF to serve as a high-quality functional interlayer with a uniform structure between the separator and LMA. In contrast, it is worth noting that the bulky polymer binder-based approach has difficulty in effectively utilizing the physical advantages of MWCNTs due to pore clogging and nonuniformity (Figure S6, Supporting Information), which deteriorates ion transfer kinetics. Specifically, the significant advantage of our approach is that the $(NH_2\text{-TAA/COOH-MWCNT})_n$ multilayers have a gapless interface with the separator due to the formation of robust interfacial interaction (i.e., hydrogen-bonding interaction) between the multilayer and the separator as well as between adjacent COOH-MWCNT layers. This phenomenon is particularly significant as it effectively excludes the possibility of needle-like Li dendrites penetrating the potential gap between the separator and the MWCF (details will be discussed later).

Furthermore, it is also very important to consider the electrical conductivity of the MWCF coated onto the separator in LMB systems. Specifically, when the lithiophilic MWCF-coated separator is in close contact with the Li metal anode, the conductive MWCF acts as an upper electrode of the LMA, enabling effective and homogeneous distribution of the current density from the separator to the Li metal anode. This means that a nanoporous MWCF with higher electrical conductivity is much more favorable for preparing high-performance LMBs with low overpotential and long-term stability. Notably, our conductive MWCF, assembled with NH_2-TAA, which has a low molecular weight (M_w ≈ 146), has a distinct advantage over MWCF with insulating NH_2-functionalized polymeric linkers (e.g., NH_2-poly(ethylene imine), NH_2-PEI). Figure 2b shows the change in the sheet resistance of $(NH_2\text{-TAA/COOH-MWCNT})_n$-coated separator and $(NH_2\text{-PEI/COOH-MWCNT})_n$-coated separator as a function of bilayer number (n). In this case, it was found that the sheet resistance value of NH_2-TAA-based separator was two orders lower (1.3×10^4 Ω sq^{-1} for $n = 3$) than that of the NH_2-PEI-based one (1.6×10^6 Ω sq^{-1} for $n = 3$). These results evidently indicate that the small molecular linker used in our approach minimizes

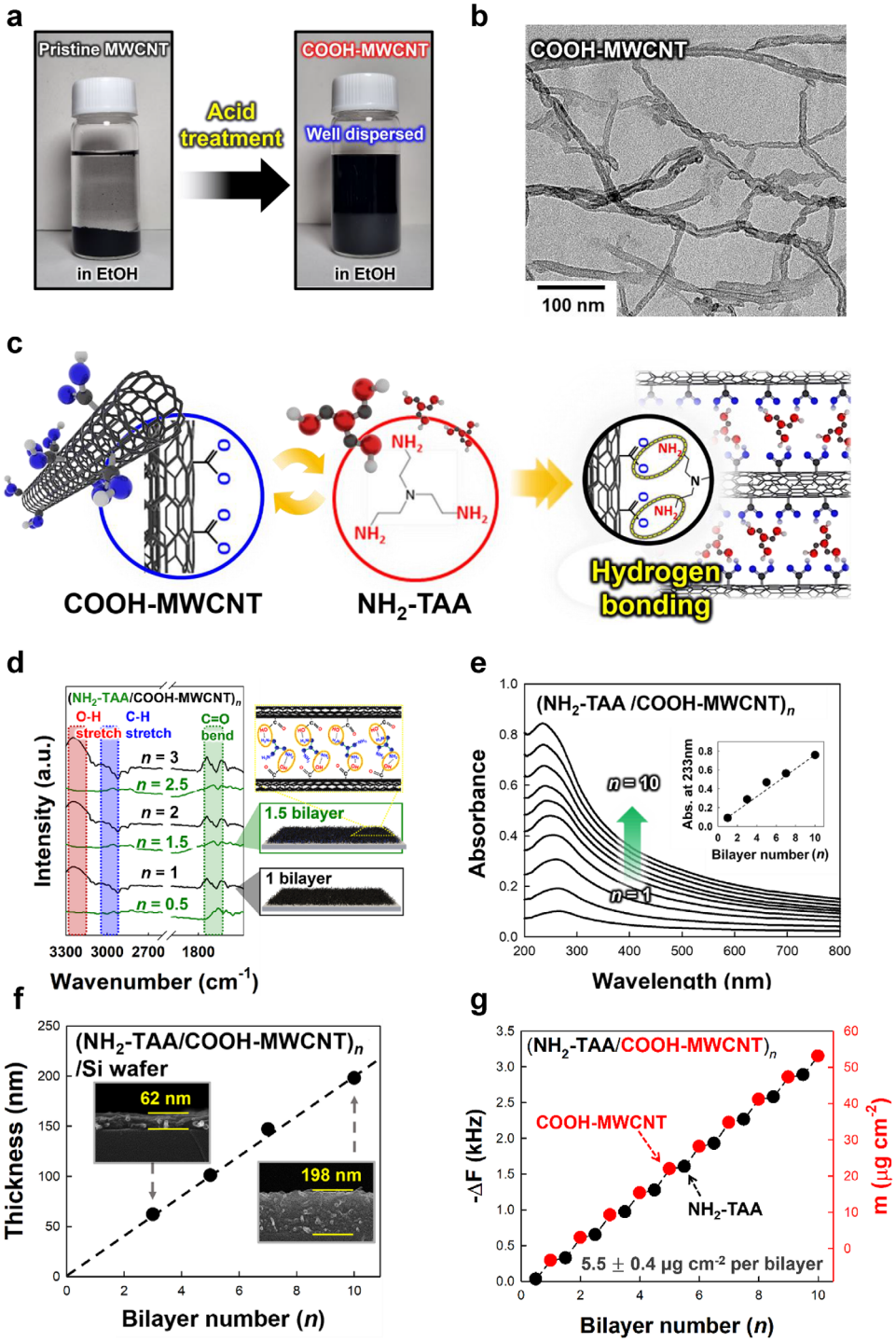

Figure 1. Preparation of *n*–MWCFs. a) Digital images of pristine (left) and acidic-treated MWCNTs (right) dispersed in ethanol. b) HR-TEM images of COOH-MWCNTs. c) Diagrams presenting the LbL assembly of COOH-MWCNT and NH_2-TAA through specific interactions. d) Changes in FTIR spectra of $(NH_2\text{-TAA/COOH-MWCNT})_n$ multilayers as a function of bilayer number (*n*). e) Variation in the UV–vis spectra of $(NH_2\text{-TAA/COOH-MWCNT})_n$ multilayers with different bilayer number (n). The inset presents the UV–vis absorbance at a wavelength of 233 nm as a function of bilayer number (*n*). f) Bilayer number (*n*)-dependent film thickness of $(NH_2\text{-TAA/COOH-MWCNT})_n$ multilayers. Insets indicate the cross-sectional FE-SEM images. g) QCM results of $(NH_2\text{-TAA/COOH-MWCNT})_n$ multilayers with different bilayer number (*n*).

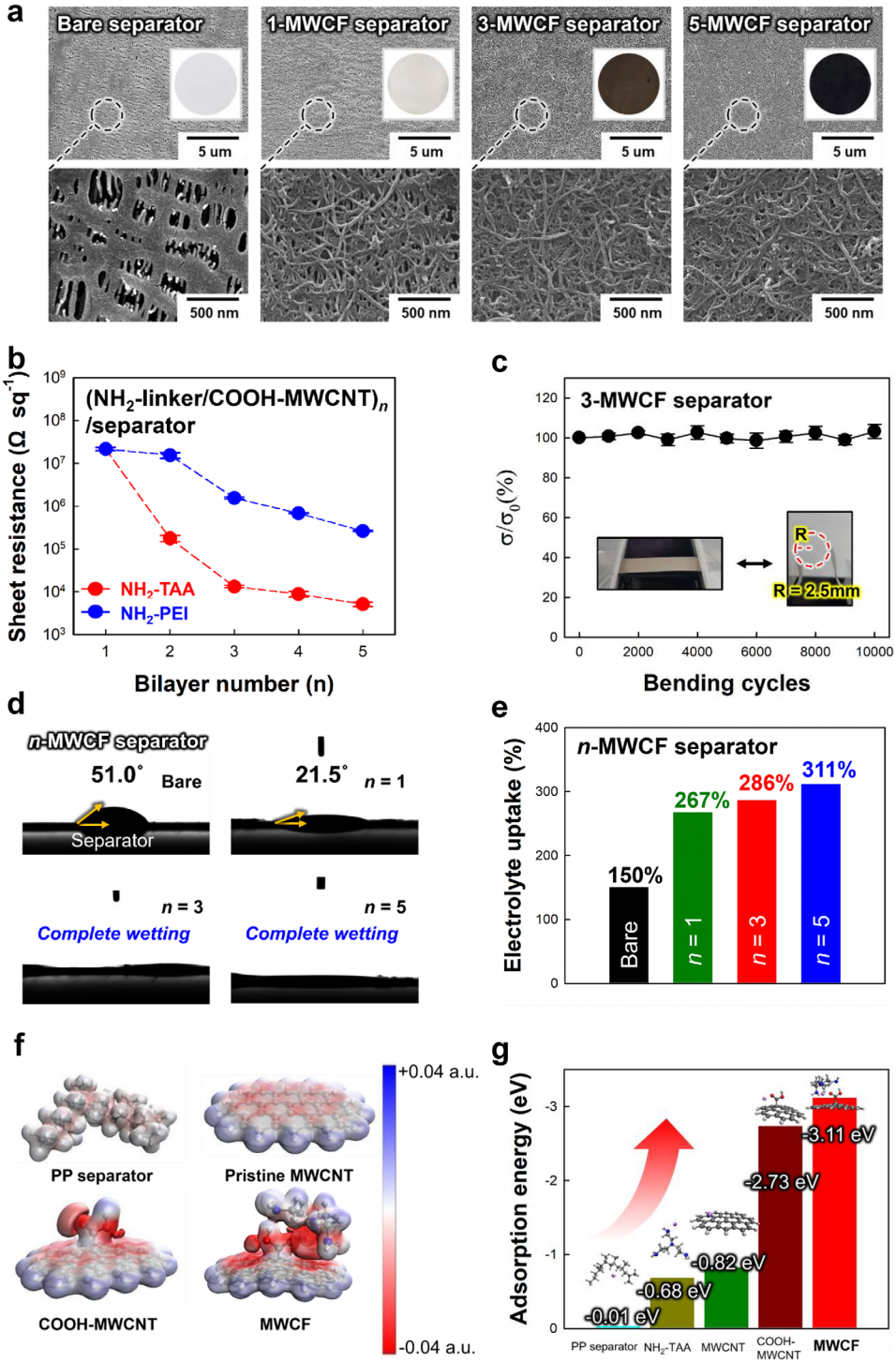

Figure 2. Characterization of *n*–MWCFs. a) FE-SEM images of *n*–MWCF separators with different bilayer numbers (*n*) of 0 (bare separator), 1, 3, and 5. The insets show the corresponding digital images of each *n*–MWCF separator. b) Bilayer number (*n*)-dependent changes in sheet resistance (Ω sq^{-1}) of *n*–MWCF separators with different linkers: NH_2-TAA (red circles) and NH_2-PEI (blue circles). c) Changes in electrical conductivity (σ/σ_0) of a 3–MWCF separator under 10 000 bending cycles with a bending radius of 2.5 mm (insets). d) Wettability tests of electrolyte (LiTFSI in DME/DIOX mixture) on *n*–MWCF separators through variations in contact angles with different bilayer numbers (*n*). e) Electrolyte uptake capabilities of *n*–MWCF separators. f) Electrostatic potential maps for the bare PP separator, pristine MWCNT, COOH–MWCNT, and MWCF, respectively. g) Trends in adsorption energy for Li^+ ions on each component.

the contact resistance between neighboring COOH-MWCNTs. Additionally, the (NH_2-TAA/COOH-MWCNT)$_3$-coated separator (abbreviated as 3−MWCF separator) exhibited excellent electrical stability even under repeated bending cycles (σ/σ_0 = 100% after 10 000 bending cycles) due to the robust interfacial interaction among all components (i.e., NH_2-TAA, COOH-MWCNT, and separator) (Figure 2c). Given that the role of the MWCF on the separator is to ensure uniform charge distribution in the interspace between the LMA and the separator, gapless interfaces between conductive MWCFs and LMA, as well as between adjacent MWCNTs, are highly beneficial for improving the performance of LMAs.

Additionally, the well-distributed functional groups within the MWCFs can ensure the good wettability of the electrolyte consisting of typical polar solvents (which usually contain oxygen molecules) in Li ion battery (LIB) applications.[41] This was confirmed by monitoring the contact angles of the electrolyte solution (1M lithium bis(trifluoromethanesulfonyl)imide (LiTFSI) in dimethyl ether (DME)/1,4-dioxane (DIOX) mixture with a 1:1 volume ratio) on the *n*−MWCF separators (Figure 2d). As the bilayer number (*n*) of *n*−MWCF separator increased from 1 to 5, the electrolyte contact angle notably decreased, ultimately reaching complete wetting in the 3−MWCF separator. In addition to such good electrolyte wettability, it should be noted that 3D-structured MWCF with numerous nanopores can serve as efficient electrolyte reservoir. When the weight of electrolyte uptake of the *n*−MWCF separator was calculated using the following Equation (1), it was increased from 150% for the bare separator to 311% for the 5−MWCF separator, respectively (Figure 2e).

$$\text{Electrolyte uptake} = \frac{W_t - W_o}{W_o} \times 100\% \quad (1)$$

where W_o and W_t represent the weight of *n*−MWCF separator before and after soaking the electrolyte, respectively. In this case, the electrolyte uptake capacity of the MWCF consistently increased with the bilayer number, indicating precise control of the specific surface area through the LbL assembly process. These results suggest that the *n*−MWCF separator has excellent electrolyte compatibility, which is highly advantageous for reducing the internal ionic resistance and achieving long-term cycle retention.[42]

Density functional theory (DFT) calculations were additionally used to gain insight into the effect of the introduced functional groups on Li dendrite formation. Based on the experimental evidence of the surface of each component on electrolyte compatibility, we compared the properties of five different representative structures: bare PP separator, NH_2-TAA, pristine MWCNT, COOH-MWCNT, and MWCF (NH_2-TAA/COOH-MWCNT multilayers) (Figure 2f; Figure S7, Supporting Information). First, we constructed the electrostatic potential (ESP) maps to visualize a charge density distribution (Figure 2f). The bare separator showed an almost neutral charge, while the pristine MWCNT without carboxyl groups displayed a slight negative charge, close to neutral. In contrast, the COOH-MWCNT showed a significant negative charge, especially localized around the oxygen atoms of the carboxyl group. Notably, extending the oxidation time of COOH-MWCNT can generate more lithiophilic carboxyl groups, but it also reduces electrical conductivity and increases the internal resistance of the cell, thereby lowering the cycle stability (Figure S8, Supporting Information). Additionally, the complementary interaction between the amine group of NH_2-TAA and the oxygen in the carboxyl group resulted in an overlap of negative charges. This visualization highlights potential adsorption sites for the Li atom.

Furthermore, the comparative analysis of the adsorption energy for Li atoms revealed distinct differences among the materials. Specifically, the bare separator, NH_2-TAA, and MWCNT exhibited weak adsorption energies of −0.01, −0.68, and −0.82 eV, respectively (Figure 2g). On the other hand, the materials containing the oxygen functional groups with significant negative charges exhibited stronger adsorption energies of −2.73 eV for COOH-MWCNT and −3.11 eV for MWCF, respectively. These results demonstrate that the NH_2-TAA acts not only as a linker but also provides additional favorable adsorption sites, effectively regulating the charge distribution for uniform Li deposition. Additionally, the atomic charge of Li tends to increase with the adsorption energy of the functional sites, indicating that the adsorption of Li atoms could be driven by a strong electrostatic interaction between the negatively charged functional site and the positively charged Li^+ ion (Figure S9, Supporting Information). Thus, DFT calculations suggest that the MWCF, with strong and uniform co-adsorption sites for Li atom, can significantly alleviate local current density and effectively prevent critical dendritic formation. Based on these findings, our approach suggests the possibility of precisely designing and controlling the functionalities of the *n*−MWCF separator through the hydrogen-bonding-mediated LbL assembly between lithiophilic COOH-MWCNTs and lithiophilic small molecular linkers (NH_2-TAAs), without incorporating any lithiophilic inactive components.

2.3. Electrochemical Properties of the *n*-MWCF Separator in a Half-Cell Configuration

To systematically evaluate the effect of the lithiophilic MWCF on Li dendrite growth behavior during Li plating and stripping processes, we assembled Li | Ni half-cells using *n*−MWCF separators with varying bilayer number (*n*). As already confirmed in Figure 2, the electrolyte wettability and uptake capacity of the MWCF vary clearly with the number of bilayers (or components), each of which induces a thickness change of ≈20 nm. This also implies that the electrochemical performance of the *n*−MWCF separator-based cell can be effectively controlled and optimized through our LbL assembly approach. Additionally, the abundant lithiophilic sites in the LbL-assembled MWCF significantly reduce the energy barrier at the initial Li nucleation step, promoting uniform Li deposition.[43] As shown in **Figure 3**a, the half-cells with the *n*−MWCF separators exhibited relatively low nucleation overpotential values compared to the bare separator-based cell. Specifically, with increasing the bilayer number (*n*) from 0 (bare separator) to 5 (5−MWCF separator), the overpotential values notably decreased from 97 to 44 mV at a current density of 0.5 mA cm^{-2}. This demonstrates a strong correlation between the bilayer number (*n*) of MWCF and its lithiophilicity.

Electrochemical impedance spectroscopy (EIS) test was further performed at room temperature to analyze the internal resistance and ion (Li^+) transfer kinetics at the interface in the

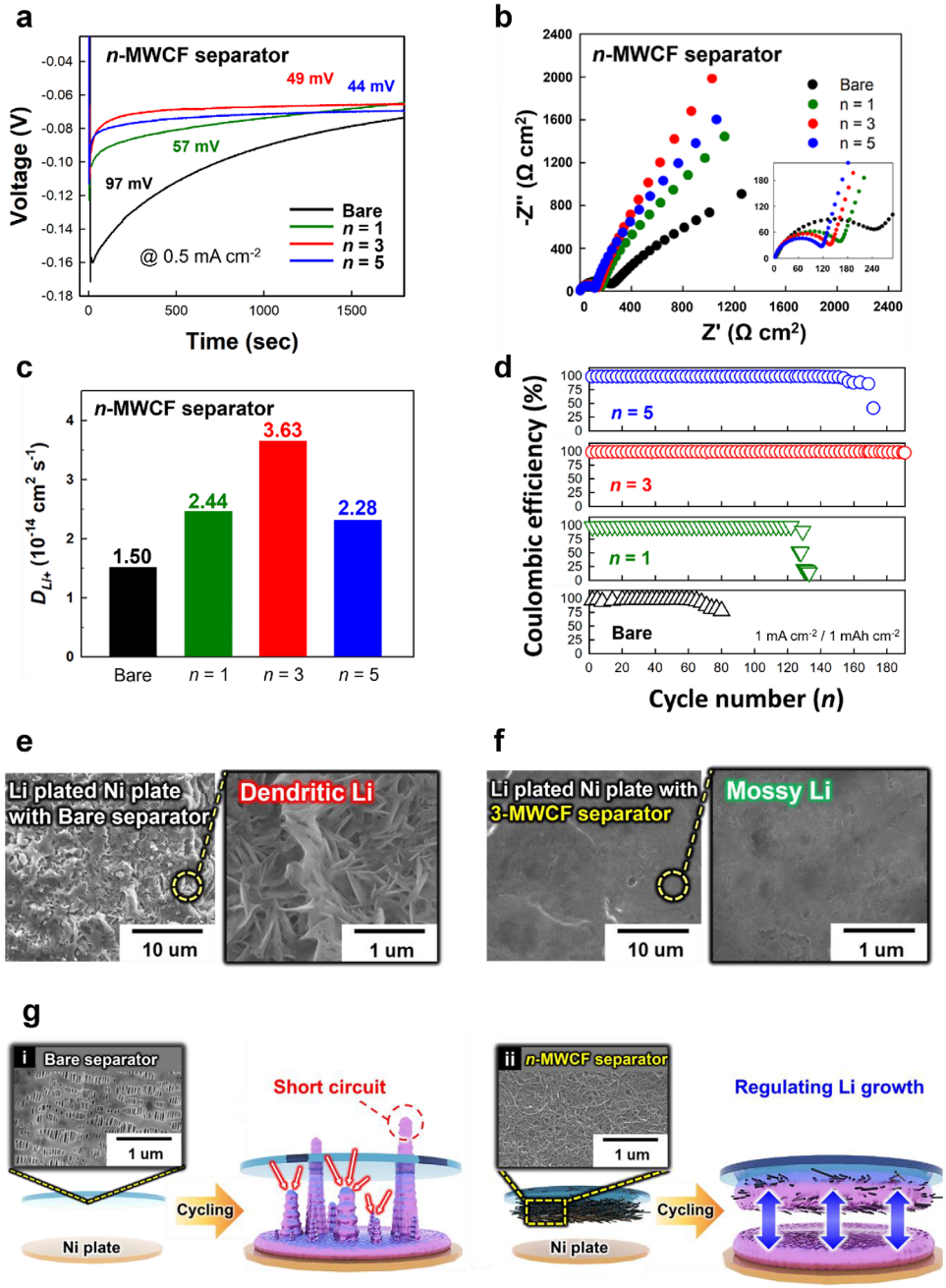

Figure 3. Electrochemical properties of *n*−MWCF separator-based half−cells. a) Voltage (V) versus time (sec) curves of *n*−MWCF separator-based Li | Ni cells during Li nucleation at 0.5 mA cm^{-2}. b) Nyquist plots for *n*−MWCF separator-based Li | Ni cells and c) the corresponding ion diffusion coefficients (D_{Li}^{+}). d) Coulombic efficiency (CE) of *n*−MWCF-based half-cells during repetitive Li plating/stripping cycles at 1 mA cm^{-2} and 1 mAh cm^{-2}. e) FE-SEM images of the surface of a Ni plate in Li | Ni cells with bare separator and f) 3−MWCF separator after cycling. g) Effect of the *n*−MWCF interlayer on Li plating mechanism in LMB systems.

n-MWCF separator-based system (Figure 3b; Figure S10, Supporting Information). In this case, the charge transfer resistance (R_{ct}) values decreased sharply from 244 (for the bare separator) to 126 Ω cm^2 (for the 101 nm-thick 5−MWCF separator), and the equivalent-series resistance (R_s) values also decreased from 7.8 to 3.8 Ω cm^2. Although ion diffusion resistance may increase with the total thickness of the *n*-MWCF interlayer, the electrical conductivity of the interlayer improved as the number of bilayers—$(NH_2\text{-TAA/COOH-MWCNT})_n$—increased from 1 to 5 (see Figure 2b). The R_{ct} value typically reflects the energy barrier associated with the de-solvation of Li^+ ions in the electrolyte, which must accept an electron from the electrode to be deposited. Therefore, the lower R_{ct} values observed in cells with *n*−MWCF separators (particularly as n increases from 1 to 3) indicate more

efficient Li^+ ion transport. This suggests that the enhanced conductivity of the interlayer reduces the activation energy required for Li^+ ion deposition, facilitating a smoother and more efficient charge transfer process.

These findings are consistent with the results presented in Figure 3a. Notably, the Warburg slope of the cell with the 5−MWCF separator—featuring a thicker and denser interlayer—was slightly lower than that of the 3−MWCF separator-based cell, indicating a modest increase in ion diffusion resistance. This phenomenon was further clarified by calculating the diffusion coefficients derived from the measured Warburg impedance (Figure 3c; Figure S11, Supporting Information). The calculated diffusion coefficients ($D_{Li}{}^+$) exhibited an upward trend as the bilayer number (n) increased from 0 to 3, but gradually decreased as the bilayer number (n) increased further from 4 to 7 (Figure S11, Supporting Information, ESI†). It is well-known that the various electrode factors, including electrical conductivity, thickness, porosity, and surface area, are closely linked to ion diffusion kinetics in electrochemical energy storage systems, thereby influencing Li dendrite growth and overall performance.[44] In this study, the LbL-assembled n-MWCF on the separator showed an increase in thickness and surface area with increasing the bilayer number (n), while the pore size gradually decreased, which was confirmed by Brunauer–Emmett–Teller (BET) analyzer (Figure S12, Supporting Information). The surface areas of bare and n-MWCF (n = 1, 3, and 5) separators were estimated to be ≈40.8, 41.4, 43.3, and 43.8 $m^2\ g^{-1}$, respectively.

To more clearly assess the influence of the n-MWCF separator on electrochemical performance of the LMBs, we monitored the Coulombic efficiency (CE) during Li plating/stripping cycles at 1 mA cm^{-2} and 1 mAh cm^{-2} in a Li | Ni half-cell configuration, depending on the bilayer number (n) (Figure 3d; Figure S13, Supporting Information). Initially, the CE of the bare separator-based cell decreased drastically after 70 cycles, indicating a short-circuit due to the uncontrollable rapid growth of Li dendrites. However, as the bilayer number (n) of the MWCF separator increased up to 3, the cycling stability was significantly improved, exhibiting a high CE of ≈97.2% after 190 cycles. Notably, this improved stability decreased again as the bilayer number was further increased from 3 to 5, consistent with the observed trends in the bilayer number-dependent ion diffusion kinetics. In fact, the Li plating behavior on the electrode surface is largely influenced by the ion diffusion condition at the electrode/electrolyte interface, which is also directly related to the dendritie growth.[45,46] Therefore, these observations suggest that the 3-MWCF separator may provide an optimal structure for effectively suppressing indiscriminate growth of Li dendrites in repeated Li plating/stripping cycles. As a result, the bare separator-based Li | Ni half-cell exhibited typical needle-like Li dendrites on the Ni plate after cycling, causing severe short-circuit (Figure 3e). In contrast, the 3−MWCF separator-based cell showed moss-like deposition of Li, as depicted in Figure 3f, indicating a well-controlled current flow over the electrode surface (i.e., Ni plate). Particularly, the enhanced ion diffusion property of the n-MWCF separator-based cell can mitigate diffusion limitations at the electrode/electrolyte interface, effectively maintaining an appropriate ion concentration for the formation of a mossy Li layer during long-term cycling (Figures S14 and S15, Supporting Information). Thus, our small molecular linker (i.e., TAA)-mediated LbL assembly can precisely tailor the functionality of the MWCF interlayer at the nanometer scale, while effectively maintaining the highly porous structure and electrical conductivity of MWCNT itself, facilitating charge transfer. In this context, the LbL-assembled conductive MWCF represents a promising alternative to insulating polymer binder-based composite interlayers. In particular, the conventional simple mechanical mixing (i.e., blending) approach, in the absence of sufficient interactions between each component, can lead to poor charge conductivity due to partial clogging of nanopores (details will be discussed later).

In addition to providing a highly porous network for efficient ion diffusion channels, the conductive MWCF interlayer with abundant lithiophilic groups serves as a robust and effective host material for stable Li plating. Specifically, a high surface coverage of the MWCF on the separator, along with the formation of a gapless interface with favorable complementary interactions, promotes the sequential deposition of Li onto the outermost surface and porous interior of n-MWCF multilayers, which is rich in lithiophilic functional groups, instead of the interface between n-MWCF and separator. This directs the Li growth from the MWCF separator to the LMA surface, effectively preventing Li dendrite penetration through the separator (Figure 3g).

2.4. Symmetric Cells Based on *n*-MWCF Separator

To precisely analyze the impact of the MWCF separator on Li deposition behavior during galvanostatic cycling, a Li | Li symmetric cell test was performed. In this test, the MWCF interlayer on the separator was held facing the working electrode (anode). After 400 cycles of Li plating/stripping at 3 mA cm^{-2}, the cell assembled with the bare separator showed typical rough dendritic growth on the Li metal anode surface (**Figure** 4a). In contrast, the 3−MWCF separator-based Li-symmetric cell exhibited very smooth and uniform Li deposition with a moss-like morphology on the Li metal surface, consistent with the observations in the half-cell configuration (Figure 4b), which ensured strong adhesion to the separator (Figure S16, Supporting Information). Importantly, the 3−MWCF, which covers the separator with a gapless interface, allows for dense Li deposition and directs the Li metal growth toward the anode surface, effectively suppressing its penetration into the bare separator (Figure S17, Supporting Information). In addition, the X-ray photoelectron spectroscopy (XPS) analysis confirmed that the SEI layer on both the 3-MWCF separator and the Li metal surface remained stable even after 400 cycles, indicating that the Li plating is uniform and well-controlled without severe morphological cracks (Figures S18 and S19, Supporting Information). Moreover, the 3-MWCF interlayer itself retained its original chemical functionalities, as evidenced by the consistent presence of characteristic functional groups in the C 1s and O 1s spectra, suggesting its structural and chemical stability during prolonged cycling (Figure S20, Supporting Information).

As mentioned earlier, the ion conduction behavior at the interface plays a crucial role in achieving stable Li plating, which is reflected in the ionic conductivity and Li^+ ion transference number of the cell.[47] To evaluate these factors, we conducted the EIS and DC polarization analysis at room temperature on Li-symmetric cells using different separators (Figure 4c; Figure S21,

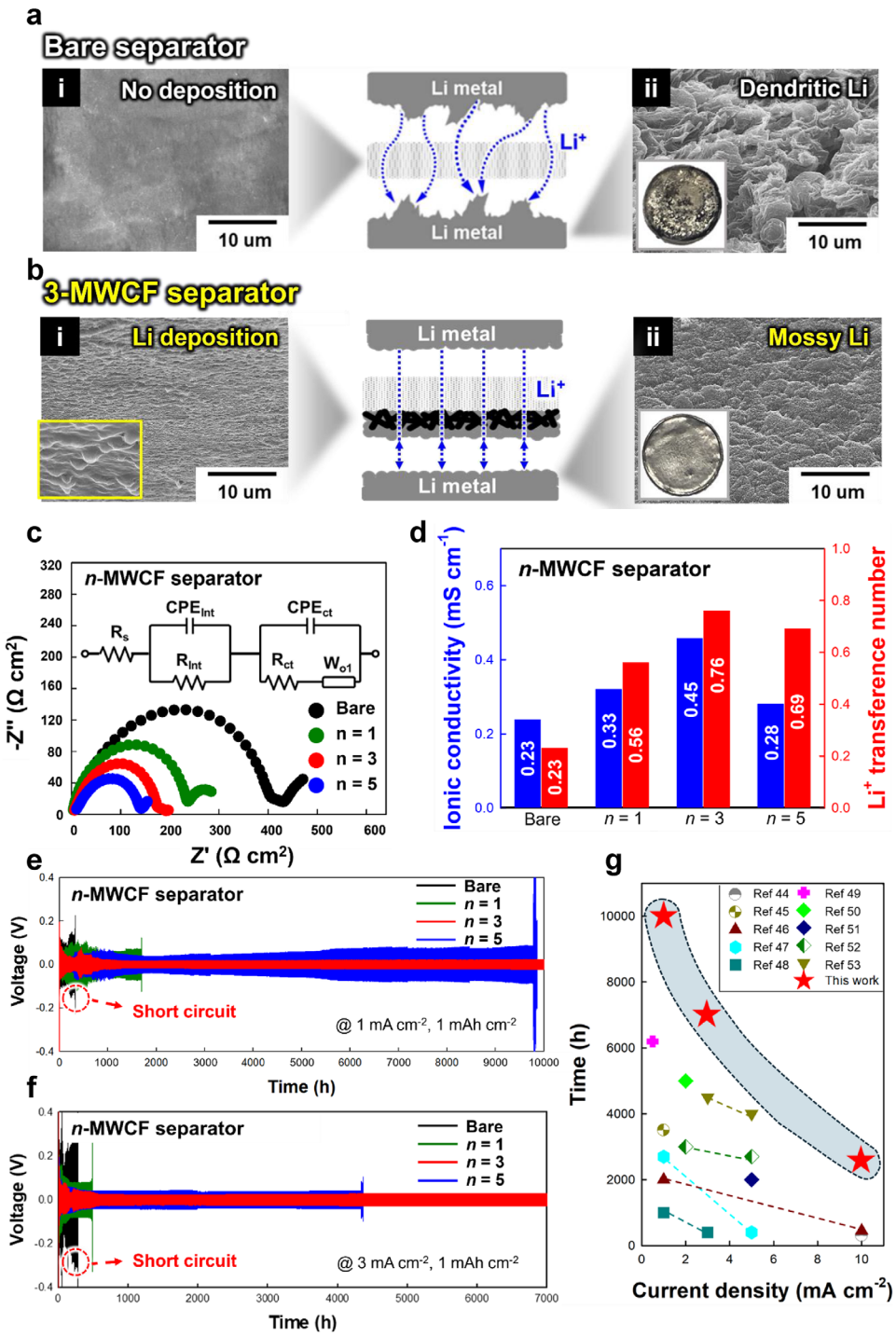

Figure 4. Symmetric cell tests. Comparison of Li plating behavior for the Li | Li symmetric cells with a) bare separator and b) 3–MWCF separator. The FE-SEM images show the surface morphologies of each separator and the Li anode. Inset indicates the digital images of the disassembled Li anodes. c) Nyquist plots and the representative equivalent circuit for *n*–MWCF separator-based Li symmetrical cells with different bilayer number (*n*). d) Ionic conductivity and Li^+ transference number of *n*–MWCF separator-based Li symmetrical cells. Galvanostatic cycling of Li symmetric cells with each separator at e) 1 mA cm^{-2} (1 mAh cm^{-2}) and f) 3 mA cm^{-2} (1 mAh cm^{-2}). g) Comparison of the cycle stability of the 3–MWCF separator-based Li symmetric cell with previous research on functional separators.

Supporting Information). In this case, the R_{ct} values of each cell notably decreased from 391.2 to 141.8 Ω cm^2 as the bilayer number (n) increased from 0 to 5 (Figure 4c). This trend aligned with the improvement in electrical conductivity of the MWCF interface with increasing bilayer number. However, despite the reduced R_{ct} value in the 5−MWCF separator-based symmetric cells, it is noteworthy that their ion conductivity and Li^+ transference number were lower compared to those of the 3−MWCF separator-based ones (Figure 4d). This observation was consistent with the trends observed in the ion diffusion coefficients and CE values of the half-cell tests. Specifically, increasing the bilayer number (n) continuously enhanced the electrical conductivity and lithiophilicity of the MWCF interlayer, but it also resulted in changes in pore size and thickness, which decreased the ion diffusion kinetics, as observed in the 5−MWCF separator-based half-cell (see Figure 3c). As a result, the 3−MWCF separator-based symmetric cell exhibited significantly higher ion conductivity (0.46 mS cm^{-1}) and Li^+ transference number (0.76) compared to other tested cells.

The superior charge diffusion properties of the 3−MWCF separator ensure uniform ion distribution at the interfaces across a wide range of current densities, thereby facilitating electrochemical reactions while effectively suppressing dendritic Li deposition. This feature can be described as "Sand's capacity (C_{Sand})," which refers to the maximum capacity at which mossy Li can form without transforming into dendritic structures. This threshold capacity is calculated by multiplying Sand's time by the current density. Sand's time is specifically defined as the period beginning with the initial deposition of mossy Li and ending when the concentration of cations (i.e., Li^+ ions) at the electrode interface decreases to zero. The relationship can be expressed by the following equation:

$$C_{Sand} = Jt_{Sand} = \pi D_{app} \frac{\left(z_c c_0 F\right)^2}{4J{t_a}^2} \quad (2)$$

where z_c is the charge number of the cation ($z_c = 1$ for Li^+), c_0 is the bulk salt concentration, F is the Faraday's constant, J is the current density, $t_a = 1 - t_{Li}$ is the transference numbers of associated anions, and D_{app} is the apparent diffusion coefficient of the electrolyte.

Based on this calculation, the Li | Li symmetric cell using the 3−MWCF separator exhibited the largest predicted regions for mossy Li formation, following the relationship $C_{Sand} = 35.2/J$ (Figure S22, Supporting Information). In addition, we investigated the interfacial stability and cycling reversibility of the n−MWCF separator-based Li-symmetric cells. To this end, the voltage profiles of the devices were monitored over long-term discharge/charge cycles at different current densities, maintaining a constant capacity of 1 mAh cm^{-2} (Figure 4e,f; Figure S23, Supporting Information). The voltage curves of all Li | Li symmetric cells using the n-MWCF separators exhibited fluctuations during the initial 200–300 h of cycling at both 1 mA cm^{-2} (under 1 mAh cm^{-2}) and 3 mA cm^{-2} (under 1 mAh cm^{-2}). Moreover, this fluctuation was more pronounced under harsher cycling conditions, such as 3 mA cm^{-2}/3 mAh cm^{-2} and 10 mA cm^{-2}/10 mAh cm^{-2}) (Figure S24, Supporting Information). This behavior may be attributed to the formation of an unstable interface between the MWCF-coated separator and the electrolyte during the early stages of cycling. In all cases, the Li-symmetric cell with a bare separator exhibited a limited life span of less than 200 cycles, accompanied by erratic voltage hysteresis. In contrast, using n−MWCF separators extended the life span of the symmetric cells with significantly reduced overpotentials. Particularly, the 3−MWCF separator-based cells showed excellent cycle stability of 5000 cycles at 1 mA cm^{-2} and 10 500 cycles at 3 mA cm^{-2}, with smooth and stable voltage plateaus showing a low voltage hysteresis below ≈28.3 mV. Moreover, to evaluate the impact of the unique structure of the 3-MWCF interlayer on enhancing cycling reversibility, the average Coulombic efficiency (ACE) was evaluated using a modified testing protocol developed by Zhang and co-workers.[48–50] After 50 cycles at a current density of 2 mA cm^{-2} with a capacity of 1 mAh cm^{-2}, the Li‖Ni cell employing the 3-MWCF separator exhibited an ACE of 99.97%, ≈0.29% higher than that of the cell with the bare separator (Figure S25, Supporting Information). Furthermore, this stable cycling behavior persisted even as the current densities and capacities increased up to 10 mA cm^{-2} and 10 mAh cm^{-2} clearly demonstrating the superior interfacial stability and Li^+ ion transfer capability of the 3−MWCF interlayer (Figure S24, Supporting Information). To our knowledge, this unprecedented high operational stability demonstrated by the 3−MWCF separator-based Li-symmetric cells significantly outperforms that of previously reported functional separator-based symmetric Li cells (Figure 4g).[51–60] Importantly, our small molecular linker (TAA)-mediated LbL design for the lithiophilic MWCNT interlayer effectively optimizes the interfacial structure to enable excellent charge conduction across a range of current densities, surpassing conventional slurry- or polymer linker-based approaches (Figures S26 and S27, Supporting Information).

2.5. Characterization of *n*-MWCF Separator-Based Asymmetric Full Cells

To further demonstrate the potential of the MWCF separator for practical LMB systems, commercially available $LiNi_{0.8}Mn_{0.1}Co_{0.1}O_2$ (NMC811) was employed as the cathode material to fabricate asymmetric full cells and characterize their electrochemical performance. The cells were tested in 1 M $LiPF_6$ in EC/DEC (1:1 by vol.%), as carbonate-based electrolytes offer superior oxidative stability, which is essential for high-voltage operation. We investigated the cycling performance of the 3−MWCF separator-based full cells (i.e., Li | 3−MWCF sep. | NMC811) with a loading amount of 1.1 mg cm^{-2} at 1 C. Remarkably, they exhibited 81.9% capacity retention and a CE of 99.9% even after 600 cycles, outperforming the bare separator-based cell, which rapidly degraded after 320 cycles (**Figure 5**a; Figures S28 and S29, Supporting Information).

To further evaluate the effect of the MWCF interlayer on the separator, we investigated the rate performance of the 3−MWCF separator-based full cells, which delivered higher capacities over a wide range of current rates compared to the bare separator-based full cells (Figure 5b). Particularly, the 3−MWCF separator-based full cells exhibited the highest specific capacity of 191.7 mAh g^{-1} at 0.1 C and 145.9 mAh g^{-1} at 2 C, which is 118% of the bare separator-based cells despite the same loading amounts of

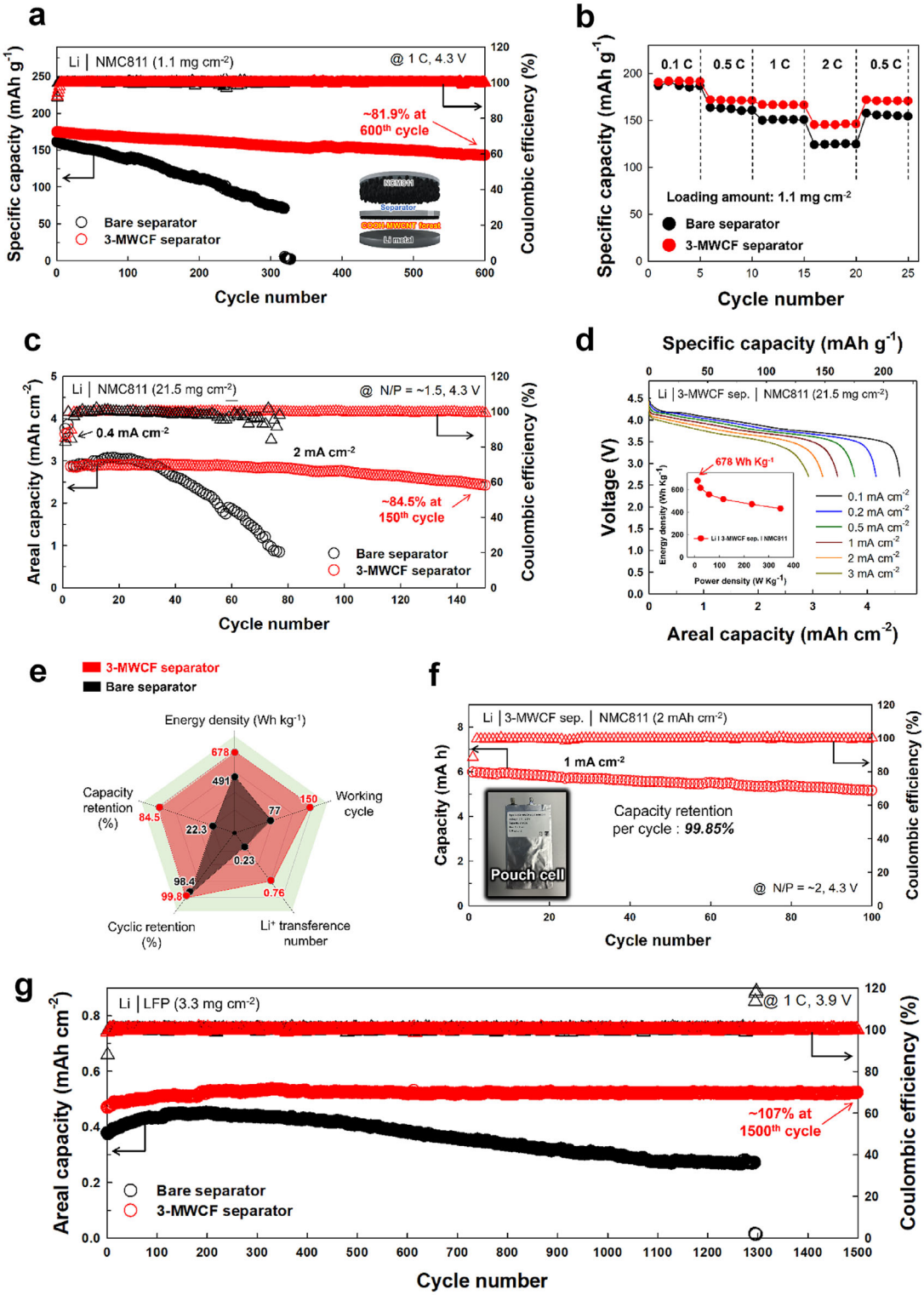

Figure 5. Performance of asymmetric full-cell with *n*-MWCF separator. a) Cycling tests of Li | NMC811 full cells with bare and 3−MWCF separators. b) Rate-capability tests of Li | NMC811 full cells with bare and 3−MWCF separators. c) Cycling tests of Li | NMC811 full cells with bare and 3−MWCF separators under a cathode loading of 21.5 mg cm^{-2} (N/P ratio ≈1.5). The tests were conducted at 2 mA cm^{-2} after precycling at 0.4 mA cm^{-2}. d) Current density-dependent discharge profiles of Li | NMC811 full cells with a cathode loading of 21.5 mg cm^{-2}. The inset presents the energy and power densities at varying current densities. e) Spider chart for Li | NMC811 full cells with different separators to compare the various performance parameters. f) Capacity retention of Li | NMC811 pouch cells with a cathode loading of 10.5 mg cm^{-2}, tested at 1 mA cm^{-2}. The inset shows a digital image of the assembled pouch cell. g) Cycling tests of Li | LFP full cells with bare and 3−MWCF separators.

active materials. This improved rate capability implies that the LbL-assembled MWCF interlayer effectively overcomes kinetic barriers and mass transport limitations at the interfaces during high-rate operation, resulting in a significant reduction in the overpotential (0.06 V) compared to that of the bare separator-based cells (≈0.3 V) (Figure S30, Supporting Information). This promising performance of the 3−MWCF separator-based full cells was further demonstrated by the EIS measurement, which showed a significantly lower R_{ct} value of 59.6 Ω cm^2 compared to 163.4 Ω cm^2 for the bare-separator-based cells (Figure S31, Supporting Information). These results clearly indicate that the 3−MWCF interlayer effectively reduces the interfacial resistance within the cell by promoting uniform Li^+ ion deposition and enhancing the Li^+ ion mobility.

Importantly, to realize high-energy LMBs in practical applications, several challenging factors must be considered, including a low capacity ratio of the negative electrode to the positive electrode (N/P ratio ≤ 2), a high cathode loading, and a reduced electrolyte content.[61] In order to clarify these critical issues, we further carried out long-term cycling tests for the full cells with a high cathode (NMC811) loading of 21.5 mg cm^{-2} and a low N/P ratio of ≈1.5 (Figure 5c). In all cases, the formation cycling was conducted at 0.4 mA cm^{-2} (0.1 C) for a stable SEI layer, then subsequently cycled at 2 mA cm^{-2} (0.5 C). As shown in Figure 5c, the 3−MWCF separator-based full cells exhibited an excellent capacity retention of 84.5% at 150 cycles, maintaining of near 100%. Afterward, the capacity dropped notably after the 200th cycle, accompanied by unstable CE, which may be due to severe Li loss (Figure S32, Supporting Information). In contrast, cells with the bare separator experienced significant capacity degradation after only 20 cycles and showed poor functionality, with CE values dropping sharply by the 77th cycle (Figure S33, Supporting Information). Additionally, the 3−MWCF separator-based full cells showed much better rate performance than the bare separator-based cells, suggesting that the improved charge conduction properties of the 3−MWCF interlayer can be particularly beneficial in mass loading applications (Figure 5d). As a result, the 3−MWCF separator-based full cells delivered the maximum energy and power densities of 678 Wh kg^{-1} and 347 W kg^{-1}, respectively, based on the total weight of active materials, significantly outperforming those of the previously reported functional separator-based cells as well as the bare separator-based cells (inset of Figure 5d).[62,63] Particularly, the excellent performance of 3−MWCF separator-based cells retained superior even when calculating the energy and power densities by including the weight of non-active components (i.e., the electrolyte, Al current collector, separator, and MWCF interlayer) as well as active materials (Figure S34, Supporting Information). Figure 5e summarizes the representative characteristics of the 3−MWCF separator-based full cells for comparison with the bare separator-based cells. These results clearly demonstrate the stable performance of the MWCF interlayer in regulating uniform current flux under rigorous practical conditions.

To expand the applicability of the MWCF separator to industrial demands, 6 mAh-level pouch cells were fabricated by employing an NMC811 cathode with an areal capacity of 2 mAh cm^{-2} (N/P ratio ≈2) and investigated for their electrochemical performance. Notably, the 3−MWCF separator-based pouch cells achieved an outstanding capacity retention of 99.85% per cycle for 100 cycles (Figure 5f; Figure S35, Supporting Information).

To further demonstrate the versatility of the MWCF separator, it was paired with LFP cathodes to construct a Li | 3−MWCF sep. | LFP full cell. The MWCF separator-based LFP cells, with a loading of 3.3 mg cm^{-2}, maintained a remarkable capacity retention of 107% even after 1500 cycles at 1 C (Figure 5g; Figures S36 and S37, Supporting Information). The gradual increase in areal capacity observed during the first 100 cycles, compared to the initial value, is likely attributed to the enlarged interfacial area between the MWCF-coated separator, LFP, and electrolyte, as well as the enhanced activation of the system through repeated cycling. This effect was particularly pronounced when using a bare separator, suggesting improved interfacial contact among the hydrophobic bare separator, the electrolyte, and the cathode components during the initial electrochemical cycling. That is, the LFP cells using a bare separator with the same loading experienced a gradual decline in capacity after 200 charge/discharge cycles. Additionally, the MWCF separator-based LFP cell with a higher cathode loading of 20.6 mg cm^{-2} exhibited a similar trend, showing a capacity retention of 96.9% after 120 cycles at 2 mA cm^{-2} (N/P ratio ≈2) (Figure S38a, Supporting Information). Furthermore, the overpotentials for the MWCF separator-based LFP cells at the 3rd and 80th cycles were 0.16 and 0.23 V, respectively, which were considerably lower than those of the bare separator-based LFP cells (0.43 V at the 3rd cycle and 0.6 V at the 80th cycle) (Figure S38b, Supporting Information). These results indicate that the LbL-assembled MWCF interlayer effectively facilitates mass transport within the cell and prevents the formation of Li dendrites. This is further corroborated by XPS analysis, which revealed that the Li metal anode paired with the 3–MWCF separator showed reduced intensities for LiF and $Li_xPO_yF_z$ compared to the bare separator. (Figure S39, Supporting Information), which was also confirmed by the atomic ratio analysis using XPS depth profile (Figure S40, Supporting Information). Additionally, the signals corresponding to stable inorganic compounds (Li_2O and Li_2CO_3) are more pronounced in the 3–MWCF separator-based anode. These phenomena suggests the formation of a thinner, more uniform SEI layer, attributed to the homogeneous Li^+ ion flux enabled by the 3–MWCF separator (Figure S41, Supporting Information). Building on this promising performance of the MWCF interlayer, the pouch cell of Li | 3−MWCF sep. | LFP with loading amount of 10.5 mg cm^{-2} with total capacity of 5 mAh (N/P ratio ≈2.3) delivered outstanding capacity retention of 99.81% per cycle at 2 mA cm^{-2} (Figure S42, Supporting Information).

3. Conclusion

We demonstrated the development of a high-performance LMB by utilizing an ultrathin MWCF interlayer assembled at the interface with the separator, effectively suppressing and directing the growth of needle-like Li dendrites during repetitive Li plating and stripping on LMAs, thereby achieving exceptional operational stability. The MWCF interlayer was LbL-assembled solely from lithiophilic COOH-MWCNTs and NH_2-functionalized molecular linkers (TAA), leveraging well-defined complementary interfacial interactions without incorporating electrochemically inactive components. This unique approach significantly enhances charge conduction properties at the interfaces while maintaining

robust structural integrity, facilitating uniform current distribution onto the LMA surface, and providing sufficient pore space for stable Li plating. Particularly, the small molecular linker-mediated LbL assembly could precisely control the chemical and physical functionalities of the MWCF interlayer on a nanometer-scale, resulting in low internal resistance and high energy efficiency even during high-rate operation.

Based on this approach, the optimized 3−MWCF separator-based symmetric cells (i.e., Li | 3−MWCF separator | Li symmetric cell) exhibited unprecedented high cycling stability of 10 500 cycles at the current density of 3 mA cm^{-2} with a significantly reduced overpotential of 28.3mV, surpassing the stability performance of the symmetric cells prepared by conventional slurry casting method. In addition, the asymmetric full cells employing the NMC811 cathode achieved a maximum energy density of 678 Wh kg^{-1} and an excellent capacity retention of 81.9% even after 600 cycles. Notably, the 6 mAh pouch cell maintained a stable capacity retention of ≈99.85% (areal capacity of ≈2 mAh cm^{-2}) per cycle. Considering that our approach can precisely control the Li dendritic growth through the multilayer functionality and structural design, we believe that it can provide a basis for the development and design of a high-performance LMB enabling ultra-long operational stability.

Supporting Information

Supporting Information is available from the Wiley Online Library or from the author.

Acknowledgements

This work was supported by the National Research Foundation of Korea (NRF) grant funded by the Korea government (Ministry of Science and ICT) (Grant No. 2021R1A2C3004151, RS-2023-00250125, RS-2024-00451691, and RS-2025-02214734), the DGIST R&D Programs of the Ministry of Science and ICT of Korea (24-ET-01), the STEAM Research Program (No. RS-2024-00421195), and generous supercomputing time from KISTI.

Conflict of Interest

The authors declare no conflict of interest.

Author Contributions

D.N., K.J., and T.H.J. contributed equally to this work. D.N., K.J., S.B., Y.K., and J.C. conceived and designed the experiments. D.N., K.J., C.L., H.Y.J., and T.H.J. conducted experiments and data analysis. K.H.K., H.K., Y.K., and S.W.L. assisted the experimental process. D.N., K.J., S.B., Y.K., and J.C. co-wrote the manuscript. All authors analyzed the results and commented on the manuscript.

Data Availability Statement

The data that support the findings of this study are available from the corresponding author upon reasonable request.

Keywords

dendritic growth, layer-by-layer assembly, lithiophilic ultrathin interlayer, lithium metal battery

Received: February 11, 2025
Revised: June 14, 2025
Published online:

[1] W. Xu, J. Wang, F. Ding, X. Chen, E. Nasybulin, Y. Zhang, J.-G. Zhang, *Energy Environ. Sci.* **2014**, *7*, 513.
[2] J. Liu, Z. Bao, Y. Cui, E. J. Dufek, J. B. Goodenough, P. Khalifah, Q. Li, B. Y. Liaw, P. Liu, A. Manthiram, Y. S. Meng, V. R. Subramanian, M. F. Toney, V. V. Viswanathan, M. S. Whittingham, J. Xiao, W. Xu, J. Yang, X.-Q. Yang, J.-G. Zhang, *Nat. Energy* **2019**, *4*, 180.
[3] Q. Wang, T. Lu, Y. Xiao, J. Wu, L. Guan, L. Hou, H. Du, H. Wei, X. Liu, C. Yang, Y. Wei, H. Zhou, Y. Yu, *Electrochem. Energy Rev.* **2023**, *6*, 22.
[4] S. Tan, Z. Shadike, X.-Q. Yang, *Electrochem. Energy Rev.* **2023**, *6*, 35.
[5] E. Cha, M. D. Patel, J. Park, J. Hwang, V. Prasad, K. Cho, W. Choi, *Nat. Nanotechnol.* **2018**, *13*, 337.
[6] K. Chen, D.-Y. Yang, G. Huang, X.-B. Zhang, *Acc. Chem. Res.* **2021**, *54*, 632.
[7] X. Gao, Y.-N. Zhou, D. Han, J. Zhou, D. Zhou, W. Tang, J. B. Goodenough, *Joule* **2020**, *4*, 1864.
[8] A. Jana, S. I. Woo, K. S. N. Vikrant, R. E. Garcia, *Energy Environ. Sci.* **2019**, *12*, 3595.
[9] R. Zhang, X.-B. Cheng, C.-Z. Zhao, H.-J. Peng, J.-L. Shi, J. Wang, F. Wei, Q. Zhang, *Adv. Mater.* **2016**, *28*, 215.
[10] C. Li, S. Liu, C. Shi, G. Liang, Z. Lu, R. Fu, D. Wu, *Nat. Commun.* **2019**, *10*, 1363.
[11] F. Hao, A. Verma, P. P. Mukherjee, *J. Mater. Chem. A* **2018**, *6*, 19664.
[12] D. Lin, Y. Liu, Y. Cui, *Nat. Nanotechnol.* **2017**, *12*, 194.
[13] K. Yan, Z. Lu, H.-W. Lee, F. Xiong, P.-C. Hsu, Y. Li, J. Zhao, S. Chu, Y. Cui, *Nat. Energy* **2016**, *1*, 16010.
[14] C. Yang, Y. Yao, S. He, H. Xie, E. Hitz, L. Hu, *Adv. Mater.* **2017**, *29*, 1702714.
[15] J. Pu, J. Li, Z. Shen, C. Zhong, J. Liu, H. Ma, J. Zhu, H. Zhang, *Adv. Funct. Mater.* **2018**, *28*, 1804133.
[16] H. Zhang, X. Liao, Y. Guan, Y. Xiang, M. Li, W. Zhang, X. Zhu, H. Ming, L. Lu, J. Qiu, Y. Huang, G. Cao, Y. Yang, L. Mai, Y. Zhao, H. Zhang, *Nat. Commun.* **2018**, *9*, 3729.
[17] L. Wang, X. Zhu, Y. Guan, J. Zhang, F. Ai, W. Zhang, Y. Xiang, S. Vihayan, G. Li, Y. Huang, G. Cao, Y. Yang, H. Zhang, *Energy Storage Mater.* **2018**, *11*, 191.
[18] S. Bai, Y. Sun, J. Yi, Y. He, Y. Qiao, H. Zhou, *Joule* **2018**, *2*, 2117.
[19] Z. Li, X. Li, L. Zhou, Z. Xiao, S. Zhou, X. Zhang, L. Li, L. Zhi, *Nano Energy* **2018**, *49*, 179.
[20] G. Lin, K. Jia, Z. Bai, C. Liu, S. Liu, Y. Huang, X. Liu, *Adv. Funct. Mater.* **2022**, *32*, 2207969.
[21] Z. Hao, Y. Wu, Q. Zhao, J. Tang, Q. Zhang, X. Ke, J. Liu, Y. Jin, H. Wang, *Adv. Funct. Mater.* **2021**, *31*, 2102938.
[22] Y. Liu, B. Yuan, C. Sun, Y. Lu, X. Lin, M. Chen, Y. Xie, S. Zhang, C. Lai, *Adv. Funct. Mater.* **2022**, *32*, 2202771.
[23] Z. Zhang, J. Wang, X. Yan, S. Zhang, W. Yang, Z. Zhuang, W.-Q. Han, *Energy Storage Mater.* **2020**, *29*, 332.
[24] M. Ali, T. Zhao, S. Iqbal, W. Zhao, H. Wang, S. Liu, S. Li, Z. Wang, Y. Ma, *J. Chem. Eng.* **2022**, *431*, 134194.
[25] L. S. Xie, G. Skorupskii, M. Dinca, *Chem. Rev.* **2020**, *120*, 8536.
[26] Z. Sun, S. Jin, H. Jin, Z. Du, Y. Zhu, A. Cao, H. Ji, L.-J. Wan, *Adv. Mater.* **2018**, *30*, 1800884.
[27] F. Liu, R. Xu, Z. Hu, S. Ye, S. Zeng, Y. Yao, S. Li, Y. Yu, *Small* **2019**, *15*, 1803734.
[28] C. Sun, A. Lin, W. Li, J. Jin, Y. Sun, J. Yang, Z. Wen, *Adv. Energy Mater.* **2020**, *10*, 1902989.
[29] G. Yang, Y. Li, Y. Tong, J. Qiu, S. Liu, S. Zhang, Z. Guan, B. Xu, Z. Wang, L. Chen, *Nano Lett.* **2019**, *19*, 494.

[30] Z. Y. Wang, Z. X. Lu, W. Guo, Q. Luo, Y. H. Yin, X. B. Liu, Y. S. Li, B. Y. Xia, Z. P. Wu, *Adv. Mater.* **2020**, *33*, 2006702.
[31] G. Wang, T. Liu, X. Fu, Z. Wu, M. Liu, X. Xiong, *J. Chem. Eng.* **2021**, *414*, 128698.
[32] Y. Liu, Q. Liu, L. Xin, Y. Liu, F. Yang, E. A. Stach, J. Xie, *Nat. Energy* **2017**, *2*, 17083.
[33] M. S. Gonzalez, Q. Yan, J. Holoubek, Z. Wu, H. Zhou, N. Patterson, V. Petrova, H. Liu, P. Liu, *Adv. Mater.* **2020**, *32*, 190636.
[34] W. Ren, Y. Zheng, Z. Cui, Y. Tao, B. Li, W. Wang, *Energy Storage Mater.* **2021**, *35*, 157.
[35] J. Pu, J. Li, Z. Shen, C. Zhong, J. Liu, H. Ma, J. Zhu, H. Zhang, P. V. Braun, *Adv. Funct. Mater.* **2018**, *28*, 1804133.
[36] W. Zhang, H. L. Zhuang, L. Fan, L. Gao, Y. Lu, *Sci. Adv.* **2018**, *4*, aar4110.
[37] H. Qian, X. Li, Q. Chen, W. Liu, Z. Zhao, Z. Ma, Y. Cao, J. Wang, W. Li, K. Xu, K. Zhang, W. Yan, J. Zhang, X. Li, *Adv. Funct. Mater.* **2024**, *34*, 2310143.
[38] Y. Hao, J. Saho, Y. Yuan, X. Li, W. Xiao, H. M. K. Sari, T. Liu, J. Lu, *Adv. Funct. Mater.* **2023**, *33*, 2212692.
[39] Y. Nie, T. Yang, D. Luo, Y. Liu, Q. Ma, L. Yang, Y. Yao, R. Huang, Z. Li, E. M. Akinoglu, G. Wen, B. Ren, N. Zhu, M. Li, H. Liao, L. Tan, X. Wang, Z. Chen, *Adv. Energy Mater.* **2023**, *13*, 2204218.
[40] Y. Li, S. Lin, D. Wang, T. Gao, J. Song, P. Zhou, Z. Xu, Z. Yang, N. Xiao, S. Guo, *Adv. Mater.* **2020**, *32*, 1906722.
[41] M. H. Ryou, Y. M. Lee, J. K. Park, J. W. Choi, *Adv. Mater.* **2011**, *23*, 3066.
[42] M. F. Lagadec, R. Zahn, V. Wood, *Nat. Energy.* **2018**, *4*, 16.
[43] X. Chen, X.-R. Chen, T.-Z. Hou, B.-Q. Li, X.-B. Cheng, R. Zhang, Q. Zhang, *Sci. Adv.* **2019**, *5*, aau7728.
[44] C. Heubner, M. Schneider, A. Michaelis, *Adv. Energy Mater.* **2020**, *10*, 1902523.
[45] P. Bai, J. Li, F. R. Brushett, M. Z. Bazant, *Energy Environ. Sci.* **2016**, *9*, 3221.
[46] A. Aryanfar, D. Brooks, B. V. Merinov, W. A. Goddard III, A. J. Colussi, M. R. Hoffmann, *J. Phys. Chem. Lett.* **2014**, *5*, 1721.
[47] B. Qiao, G. M. Leverick, W. Zhao, A. H. Flood, J. A. Johnson, Y. Shao-Horn, *J. Am. Chem. Soc.* **2018**, *140*, 10932.
[48] B. D. Adams, J. Zheng, X. Ren, W. Xu, J.-G. Zhang, *Adv. Energy Mater.* **2018**, *8*, 1702097.
[49] P. Qing, Z. Wu, A. Wang, S. Huang, K. Long, T. Naren, D. Chen, P. He, H. Huang, Y. Chen, L. Mei, L. Chen, *Adv. Mater.* **2023**, *35*, 2211203.
[50] X. Liu, K. Long, P. Qing, S. Huang, P. Xiao, C. Ling, Z. Wu, L. Chen, *Sci. China. Mater.* **2023**, *66*, 4349.
[51] D. Lee, A. Jung, J. G. Son, B. Yeom, *Energy Storage Mater.* **2023**, *61*, 102902.
[52] W. Wang, A. C. Y. Yuen, Y. Yuan, C. Liao, A. Li, I. I. Kabir, Y. Kan, Y. Hu, G. H. Yeoh, *J. Chem. Eng.* **2023**, *451*, 138496.
[53] S. Li, Q. Wang, X. Liu, H. Cui, X. Wang, Y. Xu, Z. Li, L. Wang, Z. Chen, G.-L. Xu, J. Wang, Y. Tang, K. Amine, H. Xu, X. He, *Nat. Commun.* **2022**, *13*, 172.
[54] Q. Zhang, Z. Yang, X. Gu, Q. Chen, Q. Zhai, J. Zuo, Q. He, H. Jiang, Y. Yang, H. Duan, P. Zhang, P. Zhai, Y. Gong, *Energy Storage Mater.* **2023**, *61*, 102900.
[55] S. Zheng, L. Mo, K. Chen, A.-L. Chen, X. Zhang, X. Gan, F. Lai, Q. Wei, Y.-E. Maio, T. Liu, Y. Yu, *Adv. Funct. Mater.* **2022**, *32*, 2201430.
[56] X. Li, L. Yuan, D. Liu, M. Liao, J. Chen, K. Yuan, J. Xiang, Z. Li, Y. Huang, *Adv. Funct. Mater.* **2021**, *31*, 2100537.
[57] J. Yan, F.-Q. Liu, J. Gao, W. Zhou, H. Huo, J.-J. Zhou, L. Li, *Adv. Funct. Mater.* **2021**, *31*, 2007255.
[58] Z. Hao, C. Wang, Y. Wu, Q. Zhang, H. Xu, Y. Jin, J. Liu, H. Wang, X. He, *Adv. Energy Mater.* **2023**, *13*, 2204007.
[59] S. Di, H. Li, B. Zhai, L. Li, *Proc. Natl. Acad. Sci* **2023**, *120*, 33.
[60] Z. Li, M. Peng, X. Zhou, K. Shin, S. Tunmee, X. Zhang, C. Xie, H. Saitoh, Y. Zheng, Z. Zhou, Y. Tang, *Adv. Mater.* **2021**, *33*, 2100793.
[61] S. Kim, G. Park, S. J. Lee, S. Seo, K. Ryu, C. H. Kim, J. W. Choi, *Adv. Mater.* **2023**, *35*, 2206625.
[62] M. Zhang, K. Liu, Y. Gan, H. Wang, F. Liu, M. Bai, X. Tang, Z. Wang, S. Li, A. Shao, K. Zhou, T. Wang, Z. Wang, S. Yuan, *Adv. Energy Mater.* **2022**, *12*, 2201390.
[63] S. Yao, Y. Yang, Z. Liang, J. Chen, J. Ding, F. Li, J. Liu, L. Xi, M. Zhu, J. Liu, *Adv. Funct. Mater.* **2023**, *33*, 2212466.